Mon. Not. R. Astron. Soc. **265**, 457–470 (1993)

Bipolar recurrent nova outbursts – I. Hydrodynamic models

H.M. Lloyd,[1] M.F. Bode,[1] T.J. O'Brien[2] and F.D. Kahn[3]

[1]*Chemical and Physical Sciences, Liverpool John Moores University, Byrom Street, Liverpool L3 3AF*
[2]*Computing and Mathematical Sciences, Liverpool John Moores University, Byrom Street, Liverpool L3 3AF*
[3]*Department of Astronomy, The University, Manchester M14 9PL*

Accepted 1993 June 2. Received 1993 May 27; in original form 1993 March 11

ABSTRACT

We describe hydrodynamic models of bipolar outbursts in recurrent nova systems containing a red giant with a dense wind. Two mechanisms are investigated for the production of the bipolarity observed in the outbursts of some such systems - a model in which the outburst occurs as a point explosion in an anisotropic wind, and one in which the wind is isotropic but the outburst itself is intrinsically bipolar. It is argued on the basis of radio observations of RS Oph (1985) that the latter model is more likely to be appropriate. The numerical computations of bipolar explosions also show that the ejection of parcels of gas at highly supersonic, and oppositely directed, velocities into a dense surrounding medium gives rise to bowshocks which interact in such a way as to give a dense ring of material in a plane normal to the line of ejection.

Key words: hydrodynamics – stars: individual: RS Oph – stars: mass-loss – novae, cataclysmic variables.

1 INTRODUCTION

The recurrent novae (RNe) are a small class of objects which undergo classical nova-like outbursts recurring on time-scales of a few years to decades. Within this class, however, the objects differ in both the nature of the underlying binary system and the probable outburst mechanism. In some cases, the details of the outburst are best reproduced by a thermonuclear runaway (TNR) model in which the binary system contains a white dwarf which accretes material from its companion. The outburst is initiated when nuclear burning commences under degenerate conditions within the accreted envelope, resulting in the ejection of material at velocities of up to several thousand kilometres per second. Typical outburst energies are of order $10^{42} - 10^{43}$ erg, usually lower than in classical novae, and ejected masses are in the range $10^{-7} - 10^{-6}$ $M_{\odot}$. Episodic mass transfer events have been proposed to explain the outbursts of RS Ophiuchi (Livio, Truran & Webbink 1986) and T Coronae Borealis (Webbink, Livio & Truran 1987) although, in the case of RS Oph, the existence of a constant bolometric luminosity phase during outburst and ultraviolet observations of the accretion process during quiescence indicate that the outbursts are more likely to be due to a TNR (Snijders 1987). More recently, Selvelli, Cassatella & Gilmozzi (1992) have suggested that the TNR model is also applicable to the outbursts of T CrB. Of those RNe for which there are reasonable determinations of the nature of the secondary star in the underlying binary system, four (out of the nine known RNe) contain M giants. These objects, namely RS Ophiuchi (Barbon, Mammano & Rossino 1969), T CrB (Adams & Joy 1921; Berman 1932), V745 Sco (Williams et al. 1991) and V3890 Sgr (Sekiguchi 1990; Williams et al. 1991) differ markedly from classical novae which have main-sequence dwarf secondaries and consequently a much shorter orbital period if the secondary is Roche-lobe filling. In addition, several symbiotic systems which contain red giants display nova-like outbursts. A consequence of this is that the outbursts occur at the centre of a dense red giant wind, giving rise to interactions between ejecta and circumstellar medium which are analogous to those in some supernovae. Evidence of these interactions is provided by the detection of X-rays due to hot, shocked material in the 1985 outburst of RS Oph (Mason et al. 1987), and the progressive narrowing of emission lines during outburst, seen in both RS Oph (Dufay et al. 1964) and V3890 Sgr (Gonzalez-Riestra 1992), which suggests that the nova ejecta are being decelerated by their interaction with a dense surrounding medium.

A previous series of papers (Bode & Kahn 1985; O'Brien & Kahn 1987; O'Brien, Bode & Kahn 1992) was concerned with the remnants of recurrent novae, and the 1985 outburst of RS Ophiuchi in particular. Bode & Kahn (1985) modelled the interaction between the nova ejecta and circumstellar medium by using a similarity solution to describe the dynamics resulting from the point injection of energy at the centre of a density distribution that depends on radius as $1/r^2$ and has negligible counter-pressure. O'Brien & Kahn (1987) developed these models by allowing for the effects of radiative cooling of material behind the remnant shock. Using a simplified cooling law, and treating the radiative losses as a first-order effect, they were

able to derive modified similarity solutions from linearization of the hydrodynamic equations. The X-ray emission from these models was calculated by O'Brien et al. (1992), and compared to the *EXOSAT* observations of RS Oph (1985). Although the X-ray observations (both spectra and light curves) could be modelled reasonably well using the analytical dynamics by O'Brien & Kahn, and more detailed, numerical hydrodynamic solutions (O'Brien et al. 1992), the models assumed spherical symmetry, which the radio observations of Taylor et al. (1989) would suggest is not the case. RS Oph was mapped at 1.7 GHz using three stations of the European VLBI Network on 1985 April 13, 77 d after outburst, showing clearly that the low-frequency radio emission was distributed in a bipolar structure, with two lobes roughly equidistant and on opposite sides of a bright core. Comparison of the radio and X-ray fluxes strongly suggests that much of the radio emission is non-thermal in origin, and is probably synchrotron emission. Similarly, the symbiotic system CH Cygni, which also contains an M giant secondary, underwent a nova-like outburst in 1984 which was accompanied by the appearance of a bipolar radio structure (Taylor, Seaquist & Mattei 1987). In this case, the radio observations were consistent with emission via optically thick bremsstrahlung.

Indeed, it is clear that a non-spherical outburst geometry is a common feature of recurrent and classical nova outbursts, from both spectroscopic studies [e.g. of the recurrent nova V3890 Sgr (Gonzalez-Riestra 1992) and the classical novae HR Del and FH Ser (Hutchings 1972)] and direct imaging of the remnants of old novae [e.g. DQ Her (Williams et al. 1978), RR Pic (Duerbeck 1987), HR Del (Slavin, O'Brien & Dunlop 1993)]. In this paper, we present the results of hydrodynamic modelling of bipolar nova outbursts for systems containing a red giant with a dense wind, and the subsequent interactions between ejecta and circumstellar medium. Candidates for this class of objects include the RNe RS Oph and V3890 Sgr and the symbiotic nova CH Cyg. In a paper to follow, the results of the hydrodynamic calculations are used to calculate model radio maps and X-ray spectra for comparison with the observations of RS Oph (1985), the best-studied object in this class. The physical processes that operate to produce either a bipolar nova outburst or an anisotropic red giant wind (see later) are not considered in the present papers, and we confine ourselves to a discussion of the hydrodynamic interaction of the nova ejecta with the surrounding medium, and the resulting radio and X-ray emission.

2 PHYSICAL MODELS

In order to explain the observed bipolarity of many recurrent nova outbursts, we consider two possibilities:

(i) that the outburst is spherically symmetric and the observed bipolarity results from subsequent interactions with an anisotropic red giant wind; and

(ii) that the outburst itself is intrinsically bipolar, resulting in material being ejected preferentially in the polar directions and then interacting with an isotropic ambient medium.

We will now consider these two cases in turn.

2.1 Anisotropic wind models

Here, the bipolar remnant could be produced by an ambient density enhancement in the equatorial plane. The blast wave produced by the nova event would then have a shock speed at the equator lower than that in the polar direction. This would give rise to a prolate geometry for the remnant. Similar effects are thought to be responsible for the shaping of planetary nebulae (Kahn & West 1985). In the case of planetary nebulae, such anisotropic winds can be produced in binary systems that pass through a common-envelope phase of evolution (Livio & Soker 1988), but this mechanism is inappropriate to the case of a wide binary system that contains a Roche-lobe-filling red giant, such as the objects under consideration here. However, the existence of non-spherically symmetric density distributions has been inferred around single stars and wide binaries (such as the symbiotic star R Aquarii: Henney & Dyson 1992), although the mechanism for producing this stratification is obscure. Rotation of a mass-losing star can produce a density enhancement in the equator of up to a factor of 5 (Poe & Friend 1986), but again this mechanism will not work well in the case of a red giant in which the surface velocity will be very much less than the escape velocity. For the purposes of the present paper, however, it is assumed that a polar stratification of density exists and that the mass is distributed according to a prescription due to Kahn & West (1985), which has proved successful in reproducing the shapes of planetary nebulae. The density at radius r and colatitude θ in axisymmetric spherical polar (r, θ) coordinates is given by

$$\rho(r,\theta) = \frac{\dot{M}(1+\varepsilon \sin^n \theta)}{ur^2 \int_0^{4\pi}(1+\varepsilon \sin^n \theta)\mathrm{d}\omega}. \quad (1)$$

Here, $\dot{M}$ is the total mass-loss rate into the wind in g s^{-1}, u is the wind velocity in cm s^{-1}, taken to be constant in r and θ, ω is solid angle, ε is a parameter which determines the density contrast between poles and equator and n is an integer. This form is simply a convenient expression for a density distribution resulting from a constant-velocity wind with a mass-loss rate that is higher at the equator than at the poles, and does not make any assumptions about the physical mechanism responsible for producing such a stratification.

Density distributions of this form were used by Soker & Livio (1989) in their numerical hydrodynamic calculations of the interacting winds model of planetary nebula formation (Kwok 1982; Kahn & West 1985). They found that their models could reproduce the planetary nebula shapes (round, elliptical and butterfly) in Balick's (1987) catalogue with equator-to-pole density contrasts ranging up to a factor of 16. Although some of these nebulae have binary central stars and can therefore have been shaped by common-envelope evolution, this is not the case for all the elliptical and butterfly nebulae in Balick's catalogue, and some other mechanism for producing anisotropic red giant winds must be operating. The choice of Kahn & West's density distribution for the red giant wind in these calculations is therefore reasonable in view of its success in reproducing the observed shapes of planetary nebulae.

2.2 Bipolar ejection models

In this case the bipolarity is taken to be intrinsic to the outburst. It is assumed that compact parcels of ejecta are fired in the polar directions at velocities typical of the high-velocity

systems observed spectroscopically during nova outbursts. The ejecta drive bowshocks into the red giant wind which, in the present paper, is assumed to be spherically symmetric and to have constant velocity. The density distribution in the wind is thus given by

$$\rho(r) = \frac{\dot{M}}{4\pi u r^2}. \quad (2)$$

Again, the physical processes that can produce a bipolar nova outburst in the TNR model are not clear. It is possible that the nova ejecta can be collimated into a jet by a similar mechanism to the anisotropic wind model above, although on much smaller scales than the extent of the red giant wind. In the context of the present calculations, this is equivalent to the ejection of compact blobs of material into a wind which is isotropic on scales much larger than the spatial extent of the ejecta. Calculations of this type of collimation mechanism have recently been presented by Icke et al. (1992) in their discussion of planetary nebulae.

2.3 Effects of previous outbursts

The fact that the outbursts of a recurrent nova recur on a short time-scale is important when considering the nature of the red giant wind. If it is assumed that the interaction of the ejecta and the wind results in the wind being effectively cleared away at each outburst then, at any given outburst, the wind will be of finite extent with a radius given by the product of the wind velocity and the recurrence time. It is the breaking out of the remnant shock from the confining wind that is likely to be responsible for the observed fall-off in X-ray emission from RS Oph some two months after outburst (Mason et al. 1987). This mechanism was investigated by O'Brien et al. (1992) using a numerical hydrodynamics code to calculate the evolution of the remnant beyond the edge of the wind under the assumption of spherical symmetry. A fall-off in the X-ray emission was produced by the models, but the reduction in flux was not large enough for agreement with the *EXOSAT* observations. If this mechanism is indeed responsible for the reduction in X-ray flux, the time at which the X-ray light curve begins to decay places a constraint on the extent of the red giant wind prior to outburst. Also, an upper limit of $20-30$ km s^{-1} to the velocity of the red giant wind has been given by Gorbatskii (1972), based on spectra by Dufay et al. (1964).

In both the anisotropic wind and bipolar ejection calculations presented in this paper, it is assumed that the wind is bounded by a spherical discontinuity in density. Interior to this sphere, the density is given by equation (1) or equation (2). Exterior to the sphere, the density is taken to be an uniformly low value (1 cm^{-3}). The validity of this assumption is discussed in Section 4. In all cases, we have chosen values of $\dot{M}/u$ in the range $10^{12}-10^{13}$ g cm^{-1}, in line with fits to the *EXOSAT* data on RS Oph (1985) using the spherically symmetric model by O'Brien et al. (1992).

3 HYDRODYNAMIC CALCULATIONS

We have investigated the two scenarios outlined in Sections 2.1 and 2.2 above using a numerical hydrodynamics code. The code solves the inviscid Euler equations cast in conservation law form in two-dimensional (r, z) cylindrical polar coordinates using a second-order upwind method due to Falle (1991). The conserved variables (mass density, r and z momentum density and total energy density) are discretized on a grid of uniform mesh spacing in the r and z directions. A source term is included in the r momentum equation to account for the fact that this is not a conserved quantity. Within each cell, gradients of the primitive variables (density, velocities and pressure) are calculated from the results of a half-time-step performed using Godunov's (1959) first-order method in which fluxes of the conserved variables are derived from the solution of the Riemann problems defined at the cell interfaces. These gradients are used to define new Riemann problems from which fluxes for a whole time-step are derived. The gradient in a cell is a weighted average of the gradients to the right and left of the cell centroid, and is determined using a non-linear averaging function which is chosen such that the gradients tend to zero in regions of discontinuity. This ensures that solutions remain monotonic, and that second-order accuracy in space and time is achieved in regions of smooth flow. The condition for stability is the Courant–Friedrichs–Lewy condition which constrains the time-step to a maximum value given by the minimum time for a wave to traverse one cell.

In the calculations that follow, the numerical grid has 300 cells in the r direction and 600 cells in the z direction. The active part of the grid is extended within these limits to follow the expansion of the remnant, and a conservative regridding procedure is applied when the edge of the grid is reached in a calculation. In this procedure, the dynamical variables are regridded by volume-averaging on to a grid with half the spatial resolution of the original.

In all cases, radiative losses are ignored and the calculations assume an adiabatic equation of state. This will not be the case in reality, and the effects of cooling are discussed in each case in Section 3.3. Inclusion of a radiative loss term in the energy equation poses several numerical difficulties – in cases where cooling is strong, the spatial resolution required to resolve the cooling adequately requires a large number of grid cells in each direction, making the calculations unfeasibly large. Also, since numerical shocks are spread over a number of grid cells, strong cooling can occur within the shock, giving rise to a spurious shock structure. This is easily dealt with in one dimension, but is more difficult in two dimensions where shocks pass obliquely through the grid. In all the calculations that follow, it is argued that the adiabatic approximation does not seriously affect the utility of the results for the calculation of observable quantities. In the following two sections, we discuss in turn numerical calculations of the models described in Sections 2.1 and 2.2.

3.1 Anisotropic wind calculations

The aim here is to calculate the hydrodynamic solution for a point blast at the centre of an anisotropic distribution of matter in which the density depends on radius as $1/r^2$, but with a constant of proportionality that is a function of θ. The shape of the blast wave could be calculated using any of the methods of '1.5-dimensional hydrodynamics', such as the radial flow approximation by Laumbach & Probstein (1969). However, since we are ultimately interested in calculating observables such as X-ray spectra and radio maps, we require knowledge

Table 1. Model parameters for runs A and B.

Parameter	Run A	Run B
ε	40	5
n	2	2
$(\dot{M}/u)$/g cm^{-1}	5×10^{12}	3×10^{12}
u/km s^{-1}	18.4	18.4
E_0/erg	9.33×10^{42}	1.35×10^{43}

of the detailed density and temperature profiles within the blast wave. Although a similarity solution should exist for the dynamics within the wind prior to breakout, this will not be the case at all times because the finite extent of the wind introduces a length-scale into the problem. A full numerical solution of the time-dependent equations of hydrodynamics is therefore necessary.

The density distribution used for the numerical calculations is that given by equation (1) in Section 2.1. Taking $n = 2$, and performing the integral over solid angle, we obtain

$$\rho(r,\theta) = \frac{3\dot{M}(1+\varepsilon\sin^2\theta)}{4\pi u r^2(3+\varepsilon)}. \quad (3)$$

Initially, the density is set to that given by equation (3) within a sphere of radius $R = uT$, where T is the time since the last outburst. Since we intend to compare the hydrodynamic calculations with observations of RS Oph (1985), T is taken to be 17.25 yr (the time between the optical maxima of the 1967 and 1985 outbursts of RS Oph). Outside this sphere, the number density is set equal to 1 cm^{-3}, as already stated above. The pressure is set uniformly low everywhere, such that the maximum temperature in the material is 10^4 K. All velocities are initially zero. The explosion is initiated by setting a high pressure within a small sphere (radius $\sim$ 5 grid point) at the centre of the wind, such that the total thermal energy contained within this small sphere is equal to the desired outburst energy.

The results of two calculations (hereafter run A and run B) are given here. In both cases, we have taken the radial extent of the wind to be 10^{15} cm (equivalent to $u = 18.4$ km s^{-1} for RS Oph). We have chosen density distributions with high (40, run A) and low (5, run B) density contrasts between equator and pole. Note that the high figure is much higher than required by Soker & Livio (1989) to model the shapes of planetary nebulae successfully. In both cases, the initial grid spacing is $\Delta x = 4 \times 10^{12}$ cm. The sphere of red giant wind is thus covered by 250 grid cells in each direction. The parameters for the two runs are tabulated in Table 1, in which E_0 is the total energy of the outburst. The results of the hydrodynamic calculations are shown in Figs 1 to 4. Densities and pressures are depicted by logarithmic grey-scale maps in the (r,z) plane. Velocity fields are plotted as logarithmic grey-scale maps of the magnitude of the fluid velocity, in conjunction with plots depicting the direction of the flow by means of tick marks plotted at regularly spaced intervals on the numerical grid. In the numerical calculations, one regrid was necessary for run B, whereas two were performed for run A.

The gross features of the flow in both cases are as follows. The blast wave inside the red giant wind is elongated in the polar direction, as expected for this sort of density distribution. The detailed shape of the shock wave is that of a barrel-like equatorial band with prolate extensions along the poles. Comparison of Fig. 3(a) with fig. 4(d) of Soker & Livio (1989) shows that there is good agreement between the shapes of our blast-wave solution and their interacting winds calculation using a similar density distribution ($\varepsilon = 5$, $n = 4$). The flow is roughly self-similar (see Fig. 5) – prior to breakout the equatorial and polar shock radii follow a $t^{2/3}$ time dependence but the internal dynamics and the shape of the blast-wave envelope are only approximately self-similar. This is probably due to the initial conditions, which necessarily introduce a scale-length into the problem. Only when the radius of the initial sphere of ejecta is very small compared to the size of the blast wave does the pre-breakout numerical solution tend to self-similarity.

On reaching the density discontinuity at the end of the wind, the polar shock 'breaks out' into the low-density medium exterior to this and is accelerated. The asymptotic speed reached by hot gas expanding into a vacuum is three times the sound speed prior to breakout (Pack 1953), but this speed is not reached in practice in the calculations, due to the presence of some low-density material outside the wind which is swept up by the accelerating shock. Once it has broken out, the shock tends to become spherical in the uniform-density environment beyond the discontinuity. Behind the shock, hot material streams out of the remnant into the region outside the wind. The hot gas behind the fast shock wave drives a reverse shock into this material, giving rise to a thin shell. The corrugated appearance of this shell is due to the onset of the Rayleigh–Taylor instability as the dense shell is decelerated by forward-shocked material. The initial acceleration of the polar shock at breakout and subsequent deceleration by the external medium are clearly seen for the case of run B in Fig. 5.

3.2 Bipolar ejection calculations

In order to calculate the dynamics of the remnant produced by the ejection of 'bullets' of material along the axis of symmetry into an isotropic wind, we have used the numerical code described in Section 3 with a boundary condition designed to produce supersonic jets in the polar directions. This is done by calculating fluxes at the $z = 0$ boundary such that, for radii less than some small radius r_j, the fluxes are such as to produce a supersonic flow of material in the z direction. Outside this radius, reflected symmetry obtains about the plane $z = 0$. After a certain time t_j, of order a few days, the boundary condition is changed to reflection about the whole plane $z = 0$ so that the jet is switched off, resulting in two parcels of gas moving supersonically in opposite directions along the axis of symmetry. The grid is initially filled with cold gas at rest, with the density given by equation (2) interior to a radius of 7×10^{14} cm, and equal to 1 particle per cubic centimetre outside this radius.

Figs 6 and 7 show the numerical results for a run (run C) in which the jet has an initial velocity of 3800 km s^{-1}, the ejected mass is 10^{-6} M$_\odot$ and the mass-loss rate and velocity of the wind are given by $\dot{M}/u = 8.5 \times 10^{12}$ g cm^{-1}. The bowshock driven by the bullets of ejecta can be clearly seen in Fig. 6(a), which shows the density and pressure distributions in the remnant before it has broken out of the wind. The shock does not cross the equatorial plane normally, and there is therefore an interaction of the shock wave with an identical wave which is incoming from the other side of the plane of symmetry (see

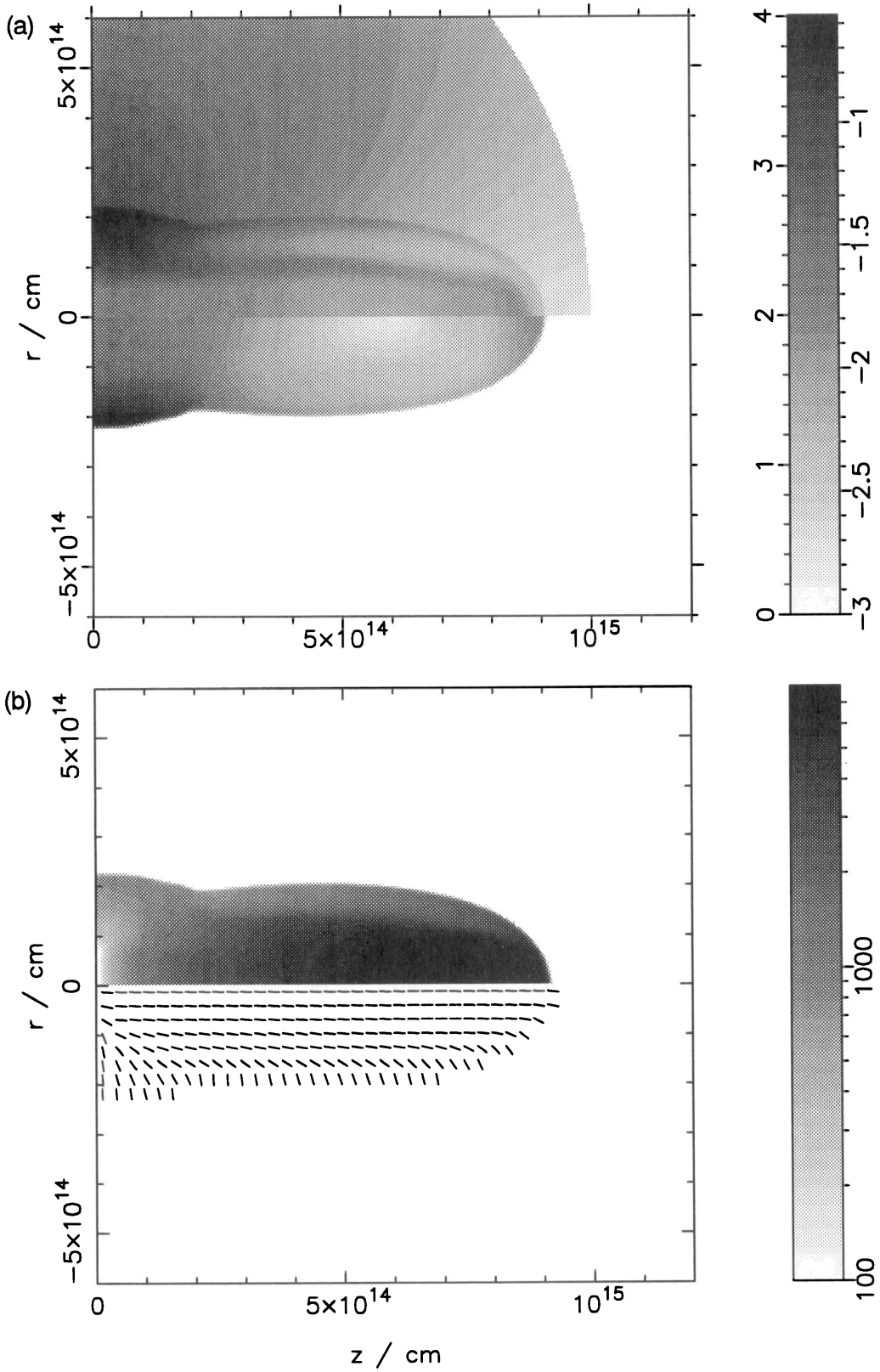

Figure 1. (a) Logarithmic density and pressure maps for run A at a model time of 11.5 d. The upper half of the plot shows the density, and the lower half the pressure. Each map shows one-quarter of the (r, z) plane, with the symmetry axis along the horizontal line through the middle of the plot. Reflected symmetry obtains about the plane $z = 0$. The key is annotated with values of $\log(\rho/10^{-20}\text{g cm}^{-3})$ on the left, and $\log(P/\text{dyn cm}^{-2})$ on the right. (b) The velocity field for run A at a model time of 11.5 d. The upper half of the plot shows a logarithmic grey-scale map of the magnitude of the fluid velocity and the bottom half shows a map of the direction of the flow field by means of tick marks drawn at regular intervals on the grid. Each map shows one-quarter of the (r, z) plane, with the symmetry axis along the horizontal line through the middle of the plot. Reflected symmetry obtains about the plane $z = 0$. The key is annotated in units of km s^{-1}.

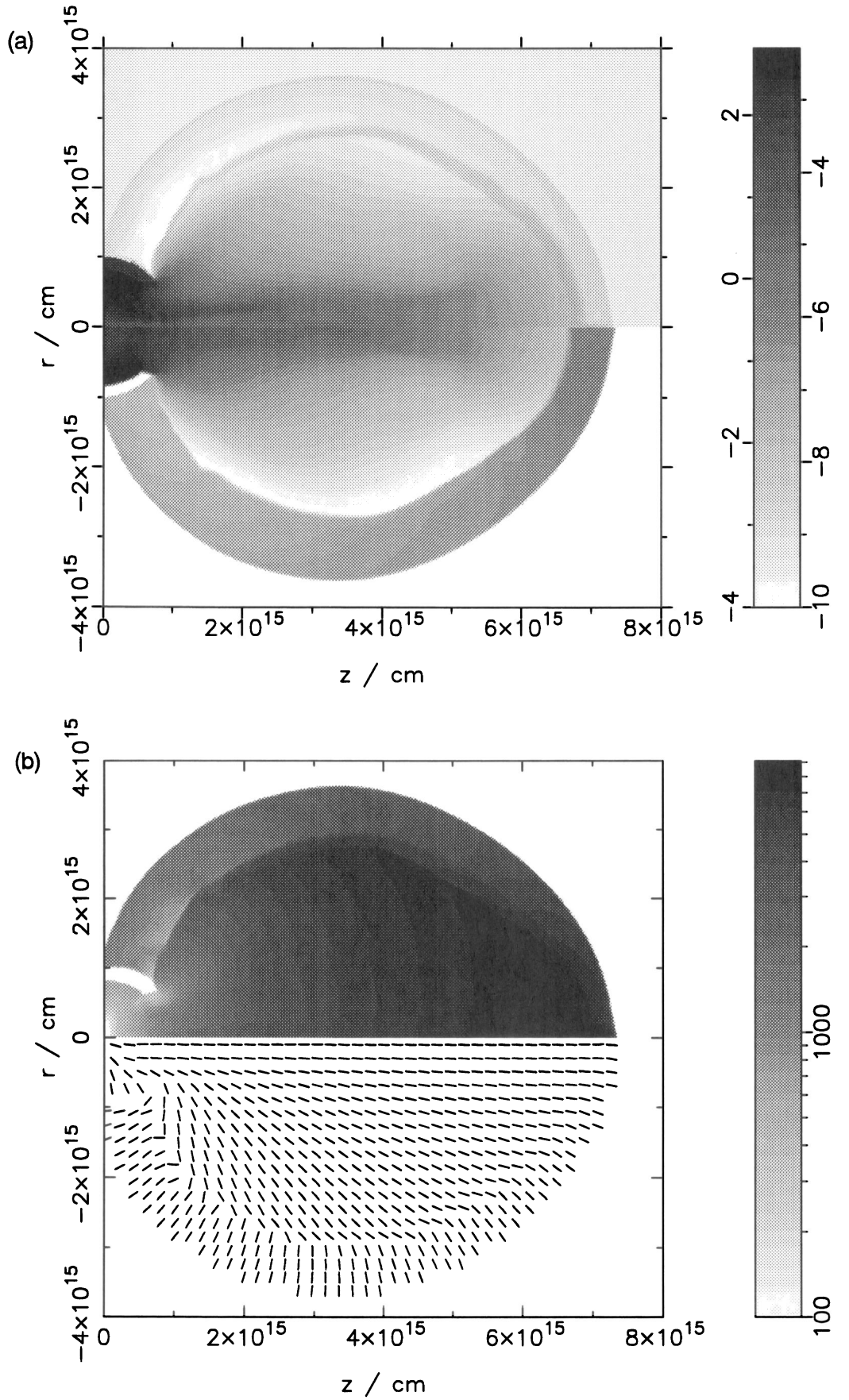

Figure 2. (a) As Fig. 1(a), but for run A at a model time of 87 d. (b) As Fig. 1(b), but for run A at a model time of 87 d.

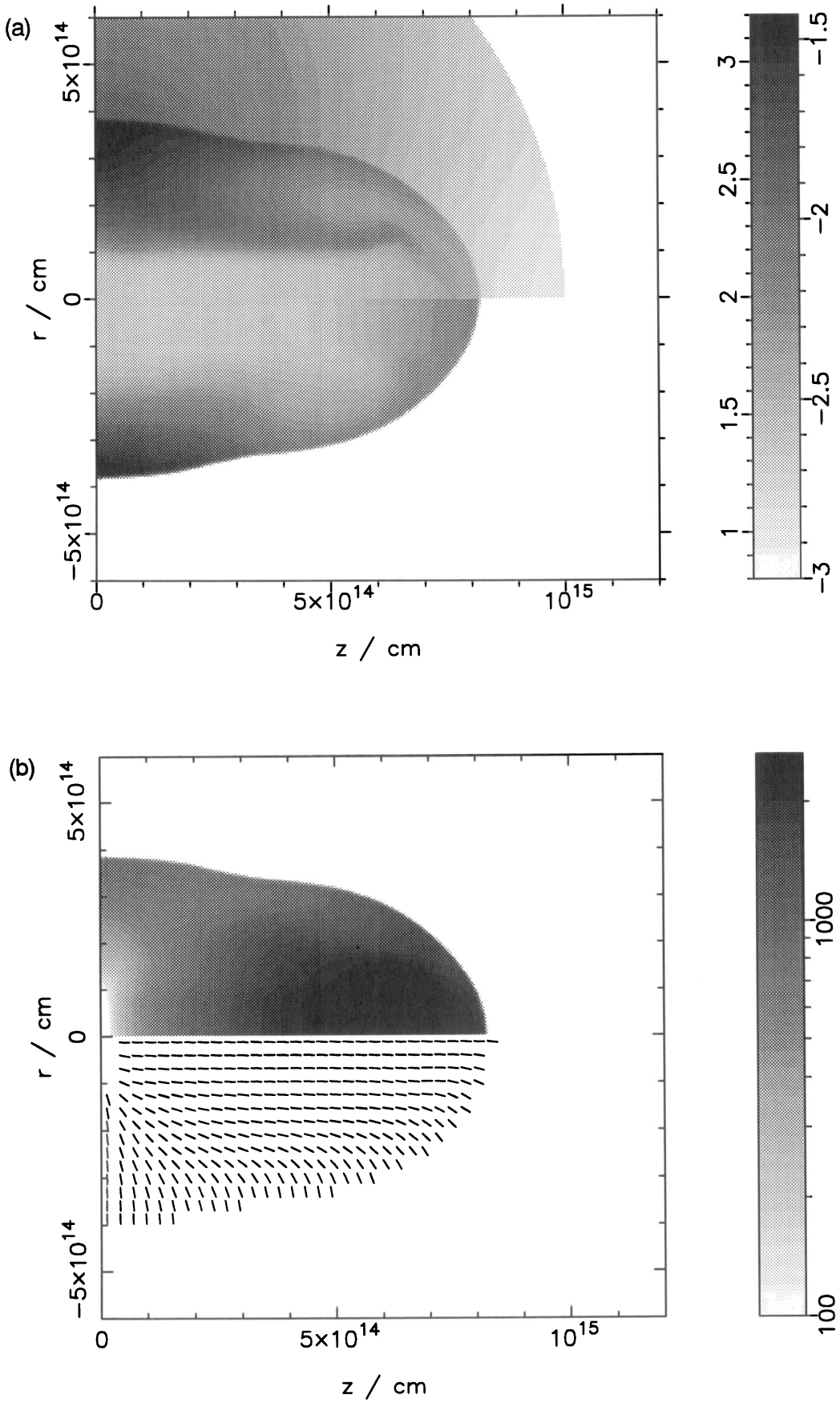

Figure 3. (a) As Fig. 1(a), but for run B at a model time of 24.2 d. (b) As Fig. 1(b), but for run B at a model time of 24.2 d.

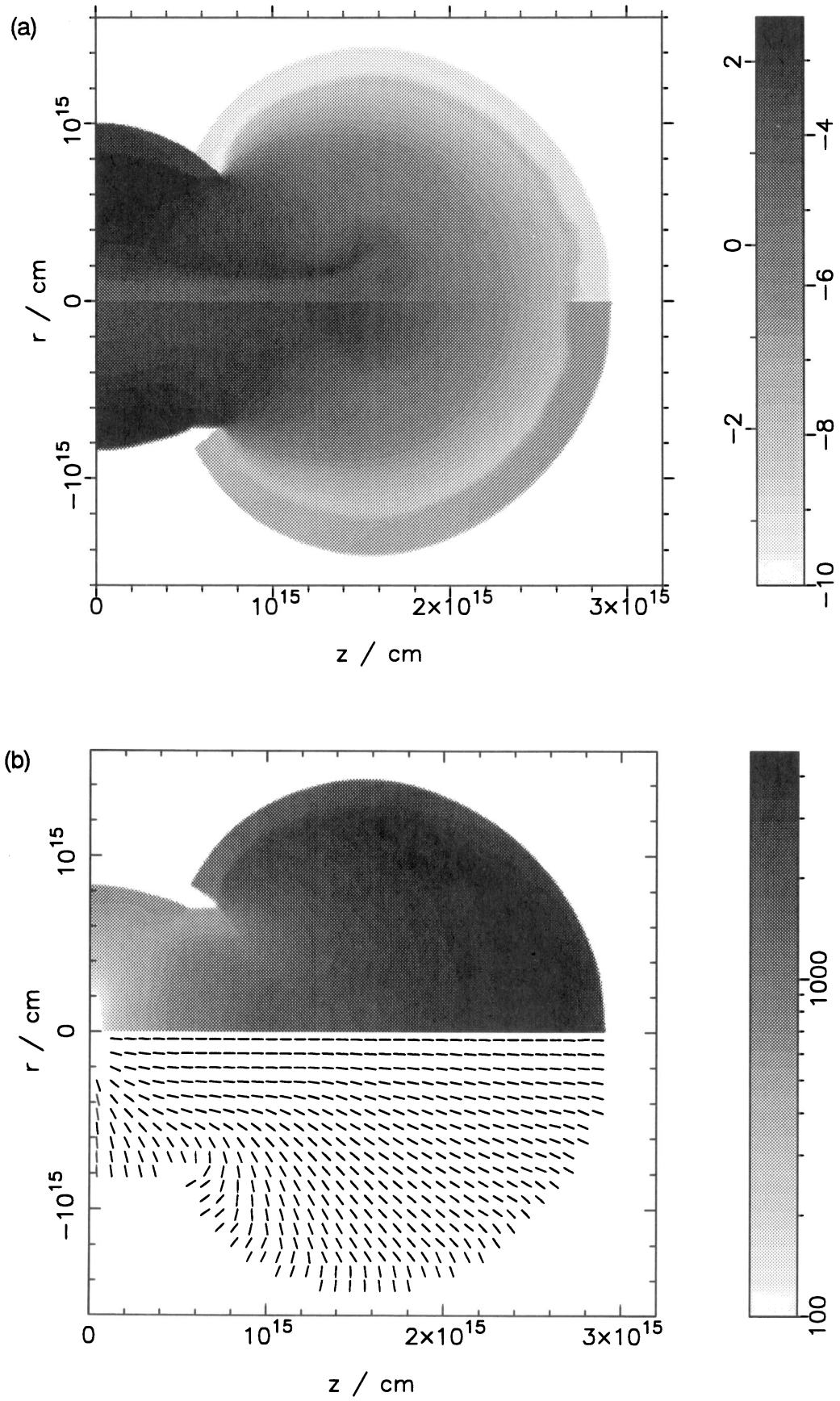

Figure 4. (a) As Fig. 1(a), but for run B at a model time of 76 d. (b) As Fig. 1(b), but for run B at a model time of 76 d.

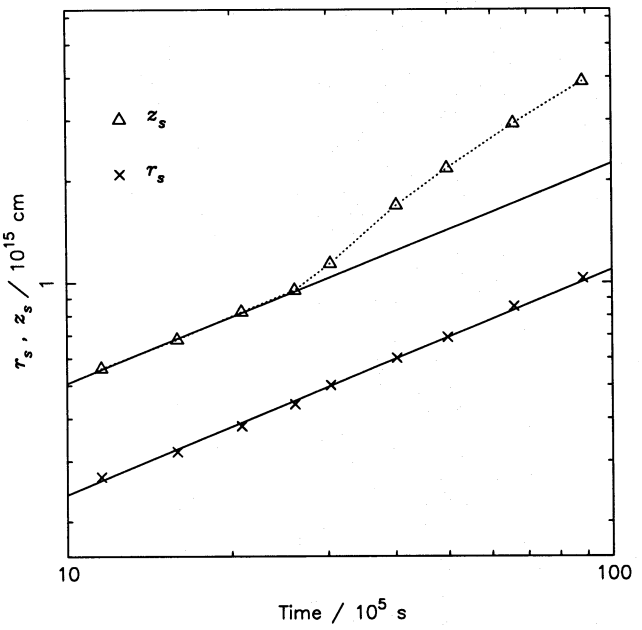

Figure 5. Log–log plot of equatorial shock radius (r_S) and polar shock altitude (z_S) against time for run B. The solid lines show the best-fitting straight lines to the points corresponding to the pre-breakout phase. The equatorial shock radius is best fitted by $r_S = 2.63 \times 10^{10} t^{0.66\pm0.01}$ cm, whereas the polar shock altitude is best fitted by $z_S = 6.46 \times 10^{10} t^{0.646\pm0.003}$ cm.

Fig. 8). The interaction gives rise to two sets of intersecting shocks on either side of the equatorial plane. The lines of intersection on either side are joined by another shock, giving rise to a pattern similar to that found in Mach reflection from a solid wall (see for example fig. 107 of Landau & Lifshitz 1987). In all cases where a single shock splits into two shocks, those leaving the intersection must enclose a tangential discontinuity. This is found to be the case in the numerical results, and is clearly seen in Fig. 8(b). The net effect of this flow is to produce a dense equatorial ring of material which is bounded by the weak shock and the tangential discontinuity. This ring can be clearly seen in Fig. 9(a), which shows the square of the gas density integrated along lines of sight at an angle of 30° to the equator. This plot depicts the appearance of the flow when viewed in the light of a radiation process in which emission measure is proportional to the square of the density.

Fig. 10 shows the equatorial and polar shock radii plotted as functions of time. It is seen that both quantities initially depend almost linearly on time and that the acceleration of the polar shock on breakout proceeds in a similar fashion to that in the anisotropic wind case. The expansion of the ring with time is best fitted by a power law in which the radius of the ring is proportional to time to the power 0.92.

3.3 Radiative cooling

In all the numerical calculations described in this paper, the energy loss due to radiative cooling has been ignored. We now consider what effect this assumption has on the numerical solutions.

In the case of the anisotropic wind solutions presented in Section 3.1, we may consider the effects of cooling by using the fact that the radius of the blast-wave shock can be written as $r = a(\theta)t^{2/3}$. The cooling time, τ_c, of post-shock gas at a particular location on the blast-wave can be written

$$\tau_c = 0.076 \frac{m_a^2 \bar{m}^{1/2}}{\lambda k^{1/2}} \frac{a^5(\theta) u (3+\varepsilon) t^{1/3}}{3\dot{M}(1+\varepsilon \sin^2\theta)}. \tag{4}$$

Here, we have used the simplified cooling law of Kahn (1976), in which the volumetric rate of energy loss is given by $\lambda \rho^2 T^{-1/2}/m_a^2$, where m_a is the mean mass of atoms and ions, T is the temperature of the gas and λ is a constant equal to 1.19×10^{-19}erg cm^3 s^{-1} for solar abundances. The mean molecular mass is $\bar{m}$ and k is Boltzmann's constant. Putting in the values of m_a, $\bar{m}$ and λ appropriate to solar abundances and noting that the cooling time is shortest at the equator ($\theta = \pi/2$), we obtain

$$\tau_c = 7150 \frac{a_{10}^5(\pi/2)}{(\dot{M}/u)_{12}} \left(\frac{3+\varepsilon}{1+\varepsilon}\right) t^{1/3}, \tag{5}$$

where $a_{10}(\pi/2)$ is the parameter a in units of 10^{10}cm s$^{-2/3}$ evaluated at $\theta = \pi/2$ and $(\dot{M}/u)_{12}$ is $\dot{M}/u$ in units of 10^{12}g cm^{-1}. The time t_* at which the cooling time becomes equal to the time since outburst is thus given by

$$t_* = \left[7150 \frac{a_{10}^5(\pi/2)}{(\dot{M}/u)_{12}} \left(\frac{3+\varepsilon}{1+\varepsilon}\right)\right]^{2/3}. \tag{6}$$

For the cooling time to be greater than, say, 80 d for evolutionary times of less than 80 d, we therefore require that

$$\frac{a_{10}^5(\pi/2)}{(\dot{M}/u)_{12}} > 5. \tag{7}$$

As long as this condition is satisfied, our adiabatic solutions will not be seriously in error. From the results of runs A and B, we obtain values of $a_{10}^5(\pi/2)/(\dot{M}/u)_{12} = 9.4$ and 22.4 respectively.

For the bipolar explosion calculations, we note that the cooling in the 'blobs' of ejecta is unimportant as far as the dynamics of the remnant is concerned. The cooling in the equatorial ring can be calculated using the result that the radius of the equatorial shock is given by

$$r = bt^{0.92}. \tag{8}$$

Again using Kahn's (1976) approximation to the cooling function between temperatures of 5×10^4 and 5×10^7 K, we can write the cooling time behind the equatorial shock as

$$\tau_c = 0.2 \frac{m_a^2 \bar{m}^{1/2}}{\lambda k^{1/2}} \frac{bt^{1.6}}{(\dot{M}/u)}. \tag{9}$$

Thus τ_c is initially smaller than t and eventually overtakes t at a time t_* given by

$$t_* = 5.43 \times 10^8 \frac{(\dot{M}/u)_{12}^{10/6}}{b_8^{25/3}}, \tag{10}$$

where b_8 is the parameter b in units of 10^8cm s$^{-0.92}$. From Fig. 10, we obtain $b_8 = 4.3$, and hence $t_* = 1$ d. Since this time is shorter than the time for which the 'jet' operates in the numerical calculations, we conclude that our adiabatic solution is a reasonable approximation to the dynamics of the remnant produced by a bipolar explosion for the parameters considered here.

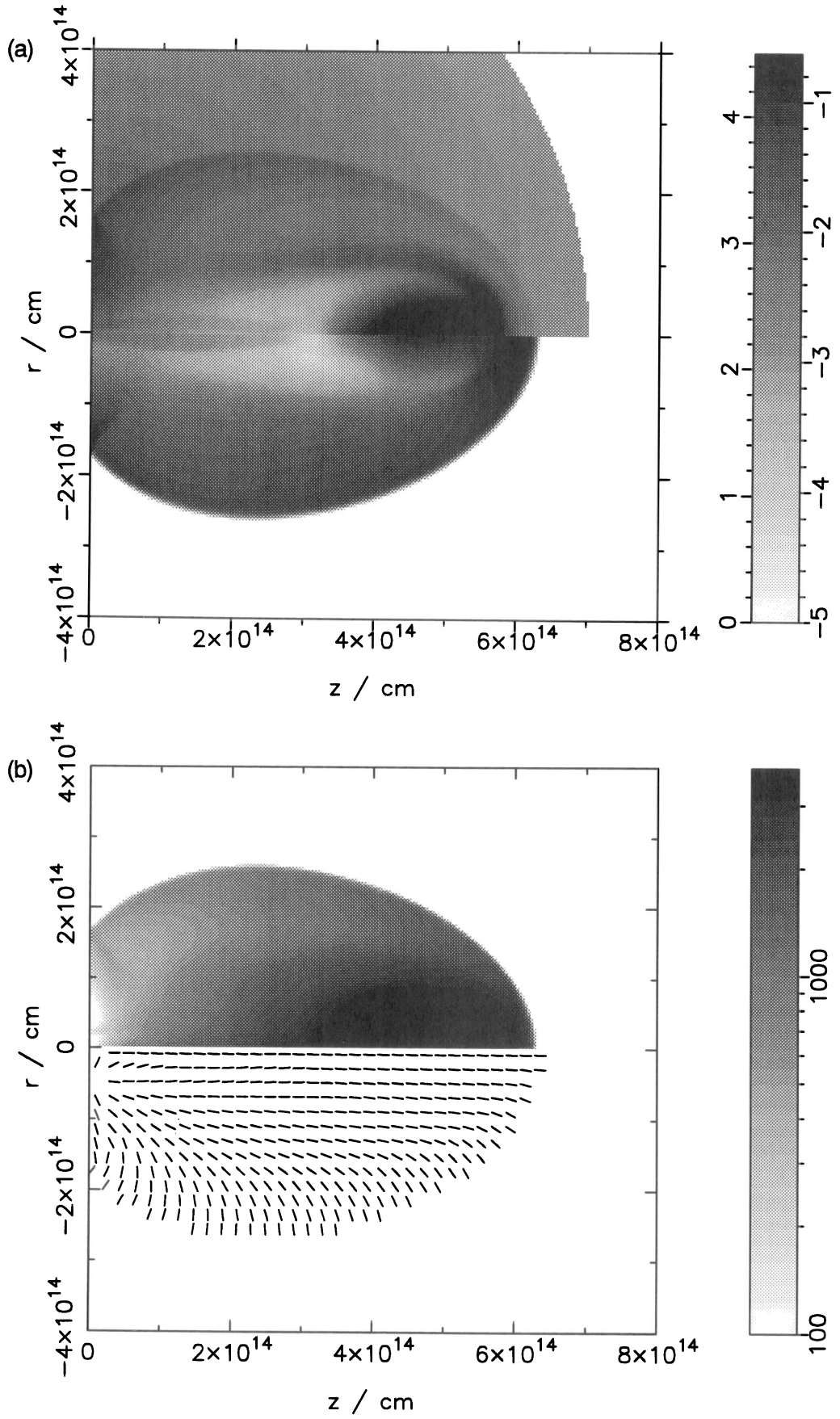

Figure 6. (a) As Fig. 1(a), but for run C at a model time of 19.2 d. (b) As Fig. 1(b), but for run C at a model time of 19.2 d.

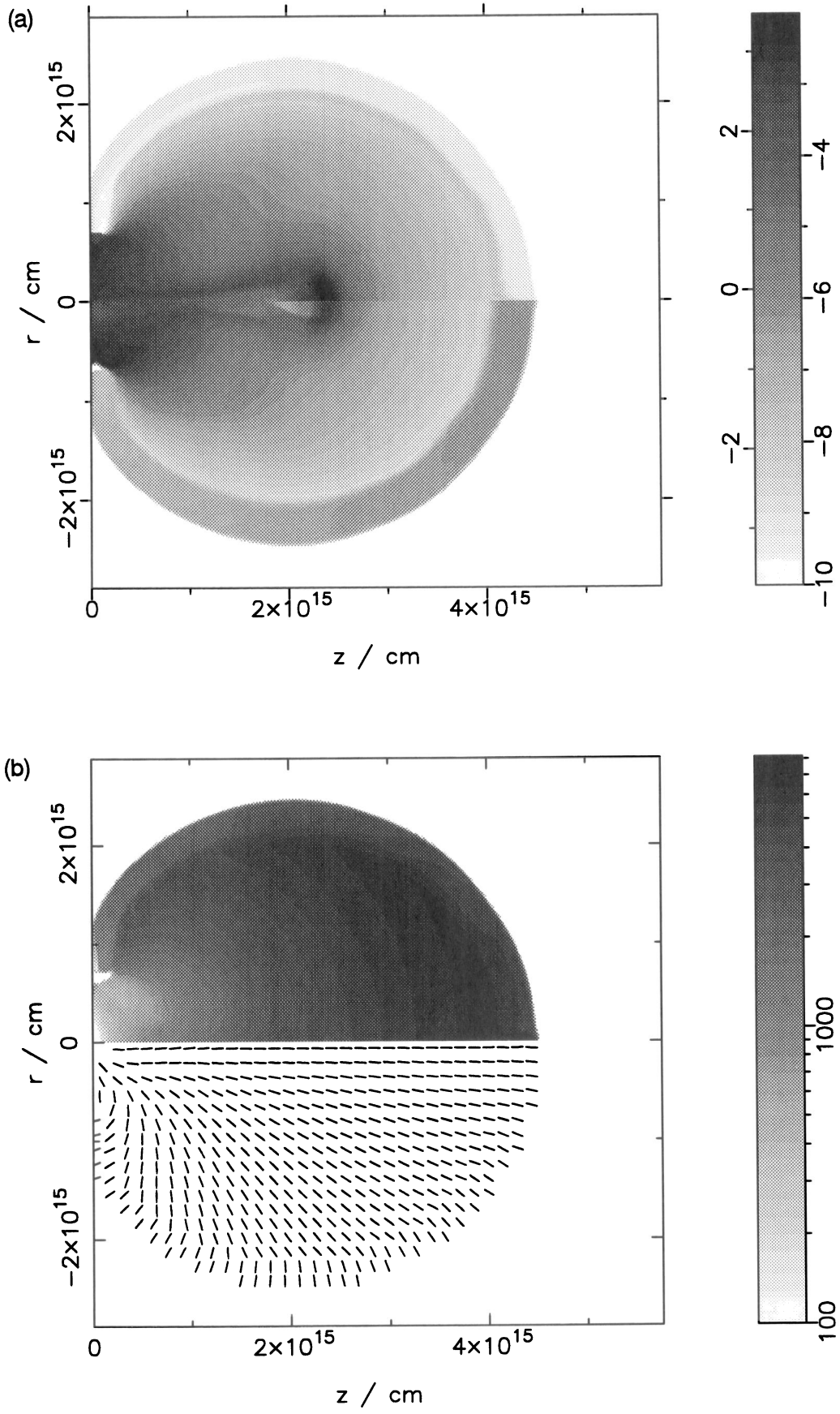

Figure 7. (a) As Fig. 1(a), but for run C at a model time of 77 d. (b) As Fig. 1(b), but for run C at a model time of 77 d.

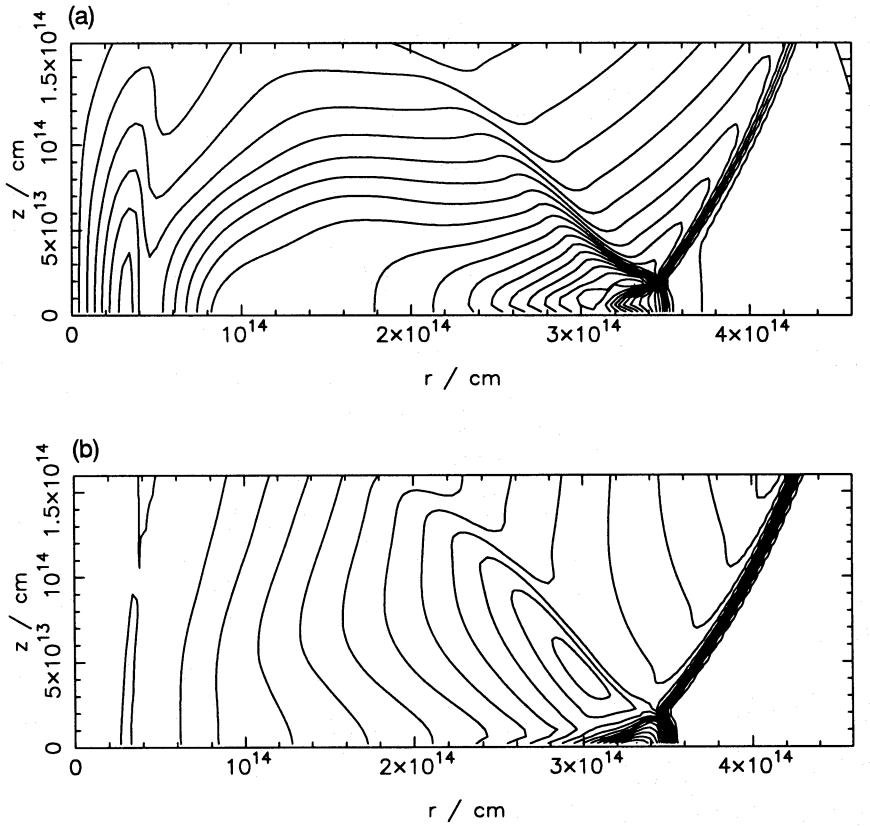

Figure 8. Detail of the shock interaction at the equator in run C. The figures show contour plots of the gas density (a) and the radial component of the fluid velocity (b).

4 DISCUSSION

We have presented the results of numerical calculations of the interaction of bipolar explosions with a dense wind. Two general cases have been considered, namely one in which the bipolarity is intrinsic to the explosion, and one in which the bipolarity is produced by the interaction of an isotropic explosion with an anisotropic wind. In the case of the intrinsically bipolar explosion, it is found that fast-moving blobs of ejecta travelling supersonically in opposite directions within a point-symmetric wind of constant velocity give rise to a dense equatorial ring of material bounded by a weak shock and a tangential discontinuity. Numerical calculations confirm that the mechanism also operates in a uniform-density environment and does not require that the surrounding medium be radially stratified. This mechanism could possibly be operating in some classical novae – such a 'polar blobs–equatorial ring' geometry is commonly found in the remnants of old novae and, although there is unlikely to be a dense wind present in these systems, this hydrodynamic mechanism will produce the observed remnant structure if the principal ejecta of the nova are highly bipolar and interact with an earlier, more symmetric phase of the outburst. In addition, Kelvin–Helmholtz instability of the tangential discontinuity would explain the fragmented appearance of many of these equatorial rings.

For the purposes of the numerical calculations, it is assumed that the wind is bounded by a spherical density discontinuity, i.e. that an outburst effectively clears away all previous wind material in the vicinity of the central binary. In all the calculations it is found that the breakout of the polar shock and streaming out of hot material do not affect the progress of the equatorial shock sufficiently to prevent it from heating the wind material in the equatorial plane when this shock is at radii $\sim 10^{15}$ cm. We conclude that all of the wind material that is built up between outbursts can be swept away by a given outburst, and our initial assumption is reasonable.

In a paper to follow, we will apply these solutions to the case of RS Oph (1985). The anisotropic wind calculations described in Section 3.1 seem to be inappropriate to RS Oph, for the following reasons. First, the radio map of RS Oph made 77 d after outburst (Taylor et al. 1989) shows two lobes on either side of a central component, each at a distance of $\sim 2.3 \times 10^{15}$ cm. It is clear that, even in the case where the density contrast between poles and equator is equal to 40, there is insufficient collimation to produce the compact lobes observed. Secondly, the equipartition energies in fast particles and enhanced fields in each lobe are 6.7×10^{39} and 4.4×10^{39}erg respectively (Taylor et al. 1989). The equipartition magnetic field strengths derived for the lobes are 0.016 and 0.030 G. This all implies an energy density in magnetic fields and relativistic electrons of about 4×10^{-5}erg cm^{-3}. This is to be compared to the thermal energy density at a distance of 2×10^{15} cm along the symmetry axis, of $\sim 10^{-6}$erg cm^{-3} in run B at a model time of 76 d and $\sim 2 \times 10^{-6}$erg cm^{-3} for run A at a model time of 87 d. If the energy densities in fast particles and magnetic fields are assumed to be equal to some fraction of the thermal energy density, then the anisotropic wind models cannot reproduce the radio observations due to the strong adiabatic cooling of

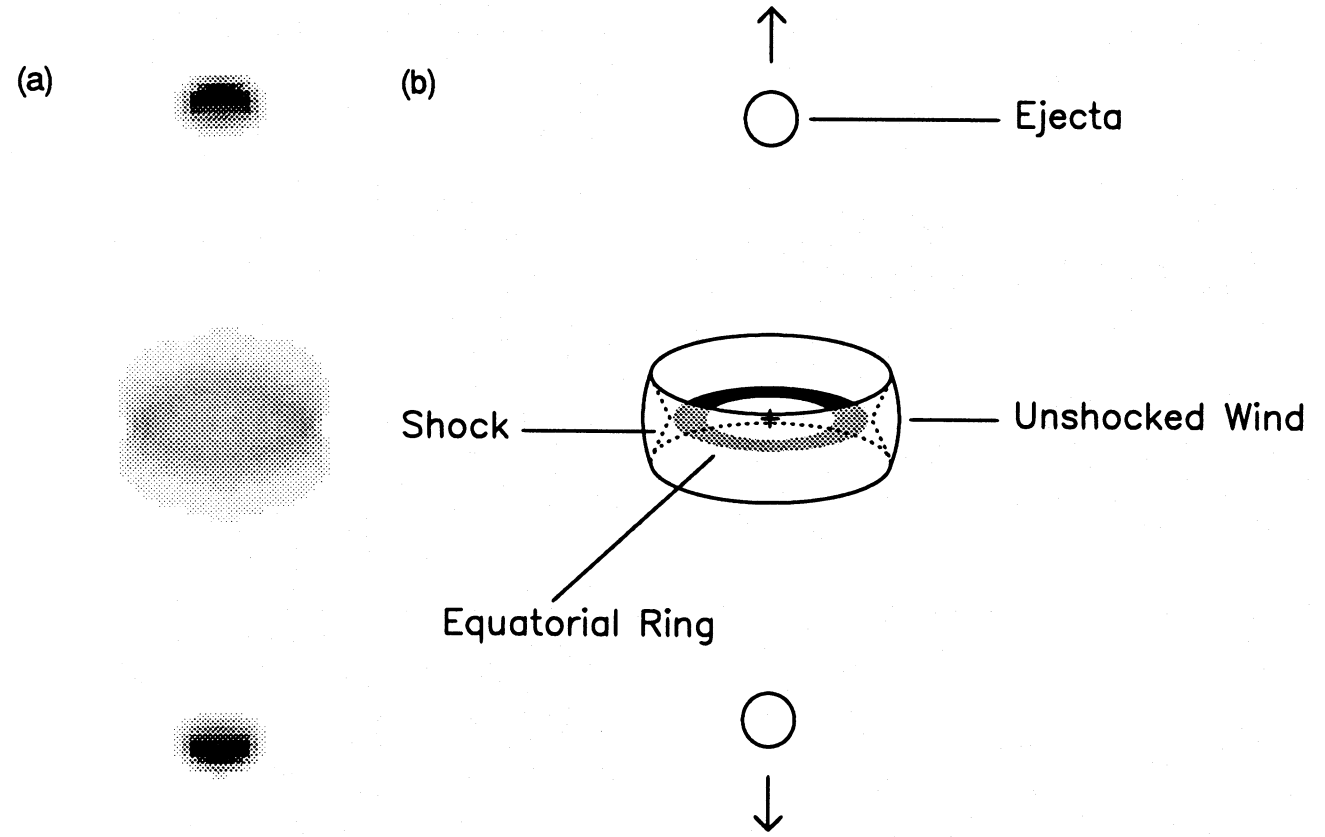

Figure 9. (a) Grey-scale plot showing the square of the gas density integrated along the line of sight for run C at 76 d. The symmetry axis is at an angle of 60° to the line of sight. The map depicts the appearance of the remnant when viewed in the light of a radiation process in which emission measure is proportional to the square of the gas density. The equatorial ring is clearly seen at the centre of the map. (b) Schematic representation of the flow pattern viewed at the same angle as in (a).

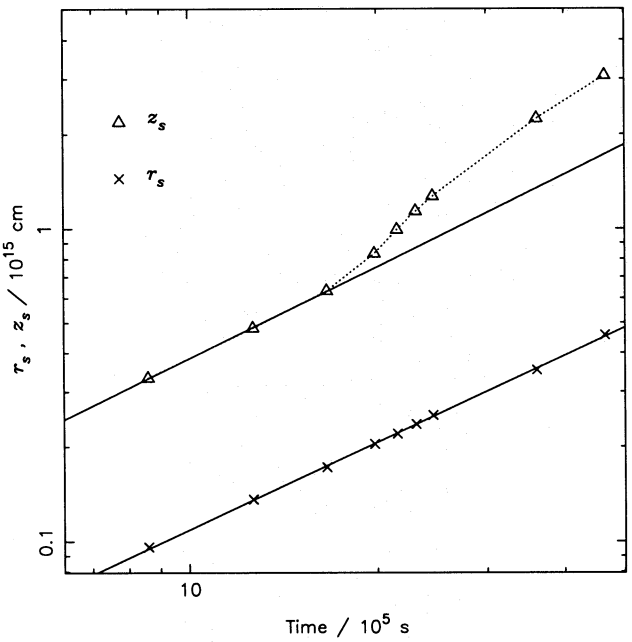

Figure 10. Log–log plot of equatorial shock radius (r_S) and polar shock altitude (z_S) against time for run C. The solid lines show the best-fitting straight lines to the points corresponding to the pre-breakout phase. The equatorial shock radius is best fitted by $r_S = 3.2 \times 10^8 t^{0.92\pm0.01}$ cm, whereas the polar shock altitude is best fitted by $z_S = 5.2 \times 10^8 t^{0.978\pm0.002}$ cm.

the material that streams out of the wind after breakout. Note that the wind speed we have used ($u = 18.4$ km s^{-1}) is close to the upper limit of 20 km s^{-1} derived by Gorbatskii (1972), so the models cannot be made to fit by increasing the wind radius, and thus collimating the flow to the required distances. It should be noted, however, that due to numerical constraints we have only considered density contrasts ranging up to 40 in the present paper. In view of the fact that the mechanism for the production of an anisotropic wind is obscure, we have no theoretical basis for an estimate of what a reasonable density contrast might be in reality, other than the requirements of models for the shaping of planetary nebulae. The conclusion that the anisotropic wind models are inappropriate to RS Oph (1985) must therefore remain tentative.

The bipolar ejection models produce compact blobs of material on either side of the central remnant, which can be identified with the radio lobes seen in the European VLBI Network map of RS Oph (1985). Models of this type therefore provide an attractive possibility of explaining the observations of RS Oph (1985). The exact nature of the radio emission that could be produced by such blobs of ejecta will depend on the details of the dynamics within the blobs. Here, we have ignored radiative cooling of the material in the blobs, since this will not affect the dynamics of the remnant within the red giant wind. However, radiative cooling will be important in determining the radio emission, because of free-free absorption if the material remains ionized. The ionization of the wind and the ejecta blobs, and the radiative cooling of the ejecta, will be

discussed in the next paper, along with the radio and X-ray emission that we would expect from the models presented here.

ACKNOWLEDGMENTS

The numerical computations were performed using the Lancashire Polytechnic Starlink Vaxcluster and the Liverpool JMU Astrophysics Vaxstation 4000. HML is supported by an SERC postdoctoral research assistantship.

REFERENCES

Adams W. S., Joy J. H., 1921, PASP, 33, 263
Balick B., 1987, AJ, 94, 67
Barbon R., Mammano A., Rossino L., 1969, in Detre L., ed., Non-periodic Phenomena in Variable Stars. Reidel, Dordrecht, p. 257
Berman L., 1932, PASP, 44, 318
Bode M. F., Kahn F. D., 1985, MNRAS, 217, 205
Duerbeck H. W., 1987, ESO Messenger, 50, 8
Dufay J., Bloch M., Bertaud C., Dufay M., 1964, Ann. Astrophys., 27, 555
Falle S. A. E. G., 1991, MNRAS, 250, 581
Godunov S. K., 1959, Matematicheskii Sbornik, 47, 271
Gonzalez-Riestra R., 1992, A&A, 265, 71
Gorbatskii V. G., 1972, Soviet Astron. AJ, 16, 32
Henney W., Dyson J. E., 1992, A&A, 261, 301
Hutchings J. B., 1972, MNRAS, 158, 177
Icke V., Mellema G., Balick B., Euderlink F., Frank A., 1992, Nat, 355, 524
Kahn F. D., 1976, A&A, 50, 145
Kahn F. D., West K. A., 1985, MNRAS, 212, 837
Kwok S., 1982, ApJ, 258, 280
Landau L. D., Lifshitz E. M., 1987, Fluid Mechanics, 2nd edn. Pergamon, Oxford
Laumbach D. D., Probstein R. F., 1969, J. Fluid. Mech., 35, 53
Livio M., Soker N., 1988, ApJ, 329, 764
Livio M., Truran J. W., Webbink R.F., 1986, ApJ, 308, 73
Mason K.O., Córdova F.A., Bode M.F., Barr P., 1987, in Bode M.F., ed., RS Ophiuchi (1985) and the Recurrent Nova Phenomenon. VNU Science Press, Utrecht, p. 167
O'Brien T. J., Kahn F. D., 1987, MNRAS, 228, 277
O'Brien T. J., Bode M. F., Kahn F. D., 1992, MNRAS, 228, 277
Pack D. C., 1953, MNRAS, 113, 43
Poe C. H., Friend D. B., 1986, ApJ, 311, 317
Sekiguchi K., 1990, IAU Circ. 5047
Selvelli P. L., Cassatella A., Gilmozzi R., 1992, ApJ, 393, 289
Slavin A. J., O'Brien T. J., Dunlop J. S., 1993, Ann. Israel Phys. Soc., in press
Snijders M.A.J., 1987, in Bode M. F., ed., RS Ophiuchi (1985) and the Recurrent Nova Phenomenon. VNU Science Press, Utrecht, p. 51
Soker N., Livio M., 1989, ApJ, 339, 268
Taylor A. R., Seaquist E. R., Mattei J. A., 1987, Nat 319, 38
Taylor A. R., Davis R. J., Porcas R. W., Bode M. F., 1989, MNRAS, 237, 81
Webbink R. F., Livio M., Truran M., 1987, ApJ, 314, 653
Williams R. E., Hamay M., Phillips M. M., Heathcote S. R., Wills L., Navarette M., 1991, ApJ, 376, 721
Williams R. E., Woolf N. J., Hege E. K., Moore R. L., Kopriva D. A., 1978, ApJ, 224, 171

This paper has been produced using the Blackwell Scientific Publications LaTeX style file.